IEEE Access
Multidisciplinary | Rapid Review | Open Access Journal

Received May 30, 2020, accepted June 17, 2020, date of publication June 22, 2020, date of current version July 2, 2020.

*Digital Object Identifier 10.1109/ACCESS.2020.3004116*

# Miniaturized Folded Ridged Quarter-Mode Substrate Integrated Waveguide RF MEMS Tunable Bandpass Filter

**THOMAS R. JONES, (Member, IEEE), AND MOJGAN DANESHMAND, (Senior Member, IEEE)**
Department of Electrical and Computer Engineering, University of Alberta, Edmonton, AB T6G1H9, Canada

Corresponding author: Thomas R. Jones (trjones@ualberta.ca)

This work was supported in part by the Canadian Research Chair Program, in part by the National Science and Engineering Research Council of Canada (NSERC), in part by the Alberta Innovates Technology Futures (AITF), and in part by CMC Microsystems.

**ABSTRACT** This paper presents a miniaturized RF MEMS tunable bandpass filter design developed by application of folded ridged quarter-mode substrate integrated waveguide cavity. Using packaged RF MEMS SP4T chips, a switchable reactive loading is applied to the folded ridged quarter-mode substrate integrated waveguide cavity, tuning the resonance frequency. Overall miniaturizations of 70.3% and 78.8% are achieved for inductively- and capacitively-loaded filters compared to an RF MEMS tunable filter using half-mode substrate integrated waveguide. Here, an analysis of inductive or capacitive loading along with their advantages and disadvantages are discussed. Two different two-pole folded ridged quarter-mode substrate integrated RF MEMS tunable bandpass filters are designed and measured. The first prototype employing inductive loading achieves 4.4% tuning range at a center frequency of 1.713 GHz, insertion loss of $3.10-3.92$ dB, and return loss greater than 15 dB for all tuning modes. The second prototype employing capacitive loading is measured with a 35.2% tuning range at a center frequency of 865 MHz, insertion loss of $1.6-4.3$ dB, and return loss greater than 10 dB for all tuning modes. The reported performance and extreme miniaturization of folded ridged quarter-mode substrate integrated waveguide cavities shows great promise for their application in tunable filter design.

**INDEX TERMS** Substrate integrated waveguide (SIW), quarter-mode, ridged, folded, RF microelectromechanical systems (MEMS), tunable bandpass filter.

## I. INTRODUCTION

Reconfigurable filters will play a critical role in future mobile communication systems, in which RF microelectromechanical systems (MEMS) based tunable elements offer superior performance in terms of insertion loss, power handling, and linearity [1], [2]. As the building blocks of filters, substrate integrated waveguide (SIW) cavities also have improved performance compared to standard planar technologies in terms of power handling and quality factor [3], [4]. In order to miniaturize the large size of SIW, technologies including half-mode SIW, quarter-mode SIW, and multilayer technologies including folded SIW, folded ridged SIW, and ridged half-mode/quarter-mode SIW have been introduced [5]–[10]. More recently, a folded ridged half-mode SIW has been presented by the authors to miniaturize SIW even further, producing a total miniaturization of 80.6% [11]. Furthermore, the authors have applied the folded ridged technique to quarter-mode SIW cavity design, with 98% miniaturization compared to standard SIW cavity [12].

The benefits of SIW cavities and packaged RF MEMS switches have previously been combined in [13], where a two-pole SIW bandpass filter achieved a 28% tuning range from $1.2-1.6$ GHz with an unloaded quality factor ($Q_u$) from $93-132$, and insertion losses from $2.2-4.1$ dB. In [14], a miniaturized two-pole half-mode SIW (HMSIW) bandpass filter was designed using packaged RF MEMS to switch between different inductive loadings along the open side of the waveguide. Comparable performance was achieved with a tuning range of 28% from $1.2-1.6$ GHz, with a $Q_u$ from $75-140$, insertion losses of $1.2-3.4$ dB, and a 60% reduction in size compared to standard SIW.

The associate editor coordinating the review of this manuscript and approving it for publication was Haiwen Liu.

In this paper, the potential of the folded ridged quarter-mode substrate integrated waveguide (FRQMSIW) is applied to RF MEMS tunable filter design to reduce the size even further, where miniaturized prototypes utilizing cavity resonators with transverse widths as small as $\lambda/16$ are demonstrated. While the authors presented a similar tunable cavity structure in [15], this work expands on the concept by providing greater detail into the principle of operation of the proposed technology, while also applying it to tunable bandpass filter design with RF MEMS tuning elements. The manuscript is organized as follows. First, in Section II, an equivalent circuit model is presented in detail for the design of reactively-loaded FRQMSIW tunable cavity resonators. In Section III, the derived analytical model is compared to the simulation of both inductively- and capacitively-loaded FRQMSIW cavities, where a packaged RF MEMS SP4T switch is used to reconfigure the reactive loading, shifting the resonance frequency. Finally, two different tunable bandpass filters are designed and measured in Section IV, using both inductively- and capacitively-loaded FRQMSIW cavities tuned using RF MEMS switches. Compared to the miniaturized HMSIW RF MEMS tunable bandpass filter reported in [13], the inductively- and capacitively-tuned filters using FRQMSIW cavity achieve additional miniaturization of 70.3% and 78.8%, respectively, highlighting the extreme amount of miniaturization possible with the proposed designs.

## II. PRINCIPLE OF OPERATION

To miniaturize the tunable HMSIW cavity presented in [14], the combination of folded ridged and quarter-mode SIW technologies with reactive loadings are investigated for tunable waveguide cavity design. A quarter-mode SIW cavity can be formed from a standard SIW cavity by cutting the waveguide into quarters along planes of symmetry of the fundamental $TE_{1,0,1}$ resonance, where due to the large width to height ratio of SIW, the open sides can be approximated as perfect magnetic conductor (PMC) walls [6]. Following this example, the authors presented a similar procedure for the miniaturization of folded ridged SIW (FRSIW) in [12], where a FRSIW cavity is cut into quarters along the planes of symmetry of the fundamental $TE_{1,0,1}$ resonance mode, forming a folded ridged quarter-mode SIW (FRQMSIW) cavity, reducing the footprint by 98% compared to standard rectangular SIW cavity.

In Fig. 1, the layout of a folded ridged quarter-mode SIW (FRQMSIW) cavity is shown, along with the (a) electric field and (b) magnetic field distributions of the fundamental quasi-$TE_{0.5,0,0.5}$ mode. The electric field magnitude is strongest underneath the ridge, and wraps around the ridge at the folding point, as shown in Fig. 1(a). The magnetic field magnitude is strongest above the ridge near the blind via, as shown in Fig. 1(b). To calculate the resonance frequency of the FRQMSIW cavity, the transverse resonance technique is applied to the equivalent circuit model in Fig. 2(a), where a PMC wall represents the open side of the cavity [12].

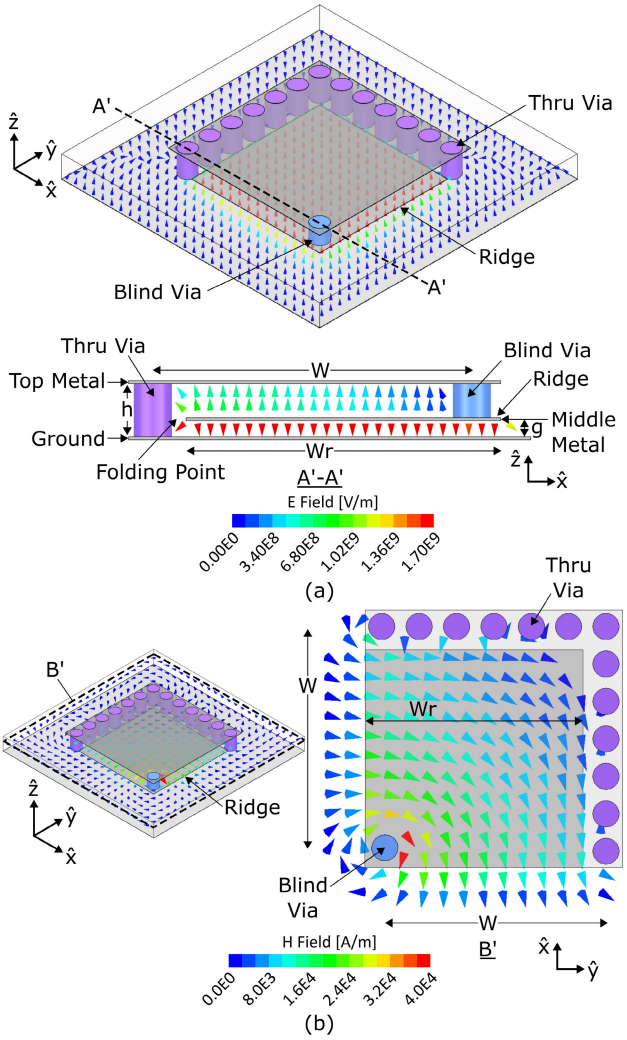


**FIGURE 1.** Layout of the FRQMSIW cavity with (a) isometric and cross-sectional view showing the fundamental electric field distribution, and (b) isometric and top view showing the fundamental magnetic field distribution.

The resonance frequency is determined by solving the following transcendental equation:

$$-cot(\frac{2\pi}{\lambda_c}W) + \frac{B}{Y_{01}} + \frac{Y_{02}}{Y_{01}}tan(\frac{2\pi}{\lambda_c}W_r) = 0 \qquad (1)$$

where $W$ and $W_r$ are the widths of the waveguide channel and capacitive ridge, respectively, $\lambda_c$ the fundamental mode resonance wavelength, $Y_{01}$ and $Y_{02}$ the transverse characteristic admittance of the waveguide channel and ridge sections, respectively, and $B$ the transverse step capacitance due to the transition between the channel and ridge at the folding point shown in Fig. 2(a).

To model a reactive loading on the FRQMSIW resonance frequency, according to the equivalent circuit diagram of Fig. 2(b), an admittance of $Y_T = Y_F + Y_{C(L)}$ replaces the PMC boundary condition used in (1), where $Y_{C(L)}$ represents either a capacitive or inductive loading, and $Y_F$ represents the fringing fields associated with the open structure.

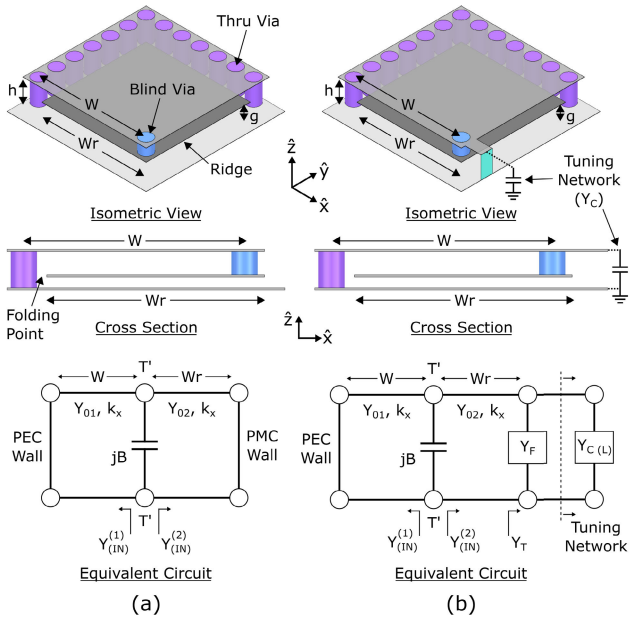


**FIGURE 2.** Isometric view, cross section, and equivalent circuit model of the FRQMSIW cavity for the (a) unloaded case with the open side modelled with a PMC wall, and (b) the PMC wall replaced with a tuning network and its physical location on the cavity.

The modified transverse resonance equation becomes:

$$-cot(\frac{2\pi}{\lambda_c}W)+\frac{B}{Y_{01}}-j\frac{Y_{02}}{Y_{01}}\left(\frac{Y_T+jY_{02}tan(\frac{2\pi}{\lambda_c}W_r)}{Y_{02}+jY_T tan(\frac{2\pi}{\lambda_c}W_r)}\right)=0. \tag{2}$$

Considering that the tuning element satisfies the condition, (2) can be simplified with the approximation $Y_{02}\gg jY_T tan(2\pi W_r/\lambda_c)$ to the following:

$$-cot(\frac{2\pi}{\lambda_c}W)+\frac{B}{Y_{01}}+\frac{Y_{02}}{Y_{01}}tan(\frac{2\pi}{\lambda_c}W_r)-j\frac{Y_T}{Y_{01}}=0 \tag{3}$$

which is the original (1), with the added loading term representing the reactive (capacitive or inductive) loading and fringing fields. This additional loading can be expressed as:

$$-j\frac{Y_T}{Y_{01}}=-j\frac{Y_F}{Y_{01}}+\frac{\omega C}{Y_{01}} \tag{4}$$

$$-j\frac{Y_T}{Y_{01}}=-j\frac{Y_F}{Y_{01}}-\frac{1}{Y_{01}\omega L} \tag{5}$$

for either capacitive (4) or inductive (5) loading.

According to (4) and (5), the loading admittance $Y_T$ is proportional to capacitance $C$, while inversely proportional to inductance $L$. Therefore, larger tuning ranges can more easily be achieved in practice using capacitive loading compared to inductive loading, due to the inherent inductance of conductive though vias. Furthermore, increased capacitive loading also decreases the resonance frequency, further miniaturizing the filter. With these considerations, the next section compares the derived analytical model with simulated FRQMSIW cavity resonators using both capacitive and inductive RF MEMS tunable loadings.

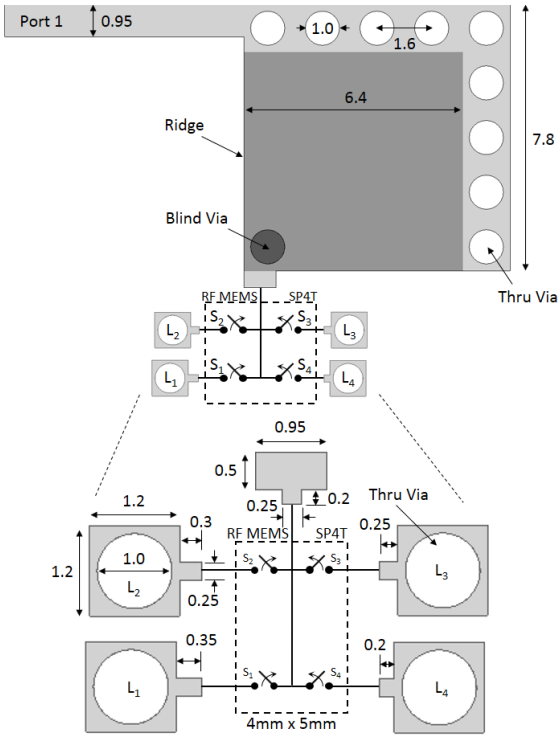


**FIGURE 3.** General schematic with dimensions of the FRQMSIW cavity resonator with packaged RF MEMS SP4T (Analog Devices, Inc. ADGM1304) to switch inductive loading (units in mm). Light and dark grey areas are the top and embedded ridge metallizations, respectively.

## III. FRQMSIW RF MEMS TUNABLE CAVITY DESIGN

In this section, the design and simulation of FRQMSIW tunable cavity resonators is presented, employing both inductive and capacitive loadings. A packaged RF MEMS switch is used to reconfigure the loading admittance seen by the resonator. The equivalent circuit model developed in the previous section is compared with simulation to verify its effectiveness in predicting the shift in resonance frequency versus reactive loading. Finally, the performance of the two loading techniques is compared and discussed.

### A. INDUCTIVELY-LOADED FRQMSIW CAVITY

In Fig. 3, the design layout of a single FRQMSIW cavity with inductive loading is shown for simulation in Keysight Advanced Design System (ADS). Rogers RO3010 is used for the top and bottom substrates, 25 mil and 10 mil, respectively. Adhesives Research EL-7876 2.2 mil thick silicone transfer adhesive tape is used as the bonding layer between the two substrates. A 50-Ω microstrip feed is weakly coupled to the resonator to extract the unloaded resonance frequency $f_0$ and unloaded quality factor $Q_u$.

An Analog Devices, Inc. ADGM1304 single-pole, four-throw (SP4T) RF MEMS switch, with low insertion loss, high linearity, and independent switch control, is used to reconfigure the inductive loading. Other benefits of the switch include actuation lifetimes reported above 1 billions cycles, hermetically sealed switch contacts, integrated driver, and an operating temperature range between 0°C to 85°C [16].

Due to a fabrication limitation, the RF MEMS chips are placed on the top substrate and connected to the top metallization layer in a location above the peak electric field location to maximize the inductive loading potential, as shown in Fig. 2(b) and Fig. 3. Conductive through via shorted to ground are chosen to provide inductive loading at the output of each switch. From (5), since the admittance of the inductive loading is proportional to $L^{-1}$, it can be seen that lower inductive loadings yield larger resonance frequency shifts. Therefore, with more inductor loadings in parallel, greater tunability can be achieved. The dimensions of the inductive loadings are given in Fig. 3. Due to the relatively large inductance inherent in conductive through via [17], the total length of each loading is very short, in order to achieve an inductance less than 5 nH for each loading. In order to include the performance of the RF MEMS chip in simulation, an Analog Devices, Inc. EVAL-ADGM1304 evaluation board is used to extract the scattering parameters of the switch itself for all the different tuning modes, i.e., with multiple switches in the ON state [16].

**TABLE 1. Switch tuning modes and simulated performance of the RF MEMS tunable FRQMSIW cavity with inductive loading.**

| Tuning Mode | S1,S2,S3,S4 | Total Inductive Loading (nH) | Tuning Element $Q$ | FRQMSIW Cavity $f_0$ (GHz) | FRQMSIW Cavity $Q_u$ |
|---|---|---|---|---|---|
| 0A | 0000 | (0.51 pF) | N/A | 1.609 | 135 |
| 1A | 1000 | 3.42 | 15 | 1.731 | 69 |
| 1B | 0001 | 3.30 | 15 | 1.734 | 71 |
| 1C | 0100 | 3.11 | 23 | 1.739 | 82 |
| 1D | 0010 | 2.99 | 19 | 1.742 | 78 |
| 2A | 1100 | 2.21 | 22 | 1.769 | 76 |
| 2B | 0011 | 2.15 | 21 | 1.772 | 73 |
| 2C | 1001 | 2.02 | 20 | 1.778 | 70 |
| 2D | 0101 | 1.90 | 23 | 1.784 | 73 |
| 2E | 1010 | 1.89 | 21 | 1.785 | 70 |
| 2F | 0110 | 1.79 | 24 | 1.791 | 76 |
| 3A | 1101 | 1.65 | 24 | 1.799 | 74 |
| 3B | 1011 | 1.64 | 23 | 1.799 | 71 |
| 3C | 1110 | 1.57 | 25 | 1.804 | 71 |
| 3D | 0111 | 1.57 | 25 | 1.805 | 74 |
| 4A | 1111 | 1.43 | 26 | 1.814 | 71 |

In Table 1, the total simulated inductive loading and quality factor ($Q$) for each switch state of the tuning element is shown. While 16 different states are achieved, since the RF MEMS switch is capacitive in tuning mode 0A, i.e., when all switches are in the OFF state, this mode is not used for the inductive loading design. Therefore, 15 unique states are used to tune the resonator. Furthermore, as additional switches are turned on, the $Q$ of the tuning element slightly increases. This is due to the series resistance $R_s$ in each switch effectively adding in parallel, and thus the total $R_s$ of the tuning element decreases, where $R_s = \omega L_s/Q$ [18].

It is generally understood that the $Q$ of a tuning element has a large impact on the overall $Q_u$ of a tunable resonator [18]. As such, Table 1 also shows the simulated $f_0$ and $Q_u$ of the inductively-loaded FRQMSIW cavity for each switch state. For tuning mode 0A, which approximates an unloaded case, the FRQMSIW cavity has a $Q_u$ of 135. However, when a single switch is turned on for tuning mode 1A, the $Q_u$ drops to 69. Thus, the $Q$ of the RF MEMS tuning element has a significant impact on the overall $Q_u$ of the FRQMSIW cavity. Nevertheless, the advantages of the RF MEMS chip make it a good choice as a tuning element for applications requiring high linearity and high power handling.

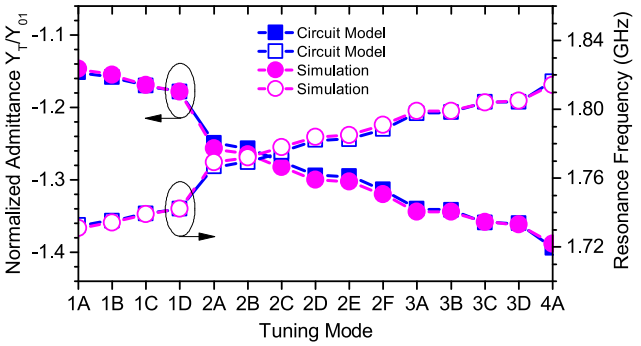


**FIGURE 4. Change in resonance frequency of an inductively-loaded FRQMSIW cavity resonator with variation in the normalized admittance for each tuning mode using the circuit model (3) and ADS simulation.**

In Fig. 4, the change in resonance frequency with variation of the normalized total inductive loading admittance $Y_T/Y_{01}$ from (3) is plotted for the different tuning modes, along with the simulated case of the loaded FRQMSIW cavity in Fig. 3. From the circuit model, the total shift in resonance frequency is 83.2 MHz at center frequency $f_0 = 1.774$ GHz, for a tuning range of 4.7%, while for the simulated FRQMSIW cavity, the shift is 83 MHz at $f_0 = 1.773$ GHz, with 4.7% tuning range.

It is noted that four main tuning states are achieved, i.e. when one switch is on, or two switches are on, etc., and within each of these main tuning states, the impact of the specific switch used yields only a small change in resonance frequency. While the inductive loadings for each switch were designed to have successively larger values by having longer lengths, as seen in Fig. 3, it was found that the internal inductance (ON state) and internal capacitance (OFF state) of the RF MEMS chip itself was different for each path. Regardless, good agreement between the circuit model and simulated model is shown, validating the analytical theory developed in Section II. Furthermore, the small shift in resonance frequency within the four main tuning states can be used for fine-tuning due to fabrication tolerances.

For the inductively-loaded FRQMSIW cavity above, the small tuning range of 4.7% is due to the inverse relationship between loading admittance and inductance shown in (5), and the difficulty in realizing small inductance values in practice. While other benefits exist for the use of inductive loading, such as a wider spurious-free region above the passband or fine tuning of the filter post-fabrication (discussed in more detail in Section IV), the capacitive loading of a simulated FRQMSIW cavity is now explored.

### B. CAPACITIVELY-LOADED FRQMSIW CAVITY

In Fig. 5, the design layout of a single FRQMSIW cavity with capacitive loading is shown for simulation in ADS. Rogers RO3010 is again chosen, however, thicker substrates 50 mil and 25 mil are used for the top and bottom, respectively, to improve the resonator's quality factor, while keeping the

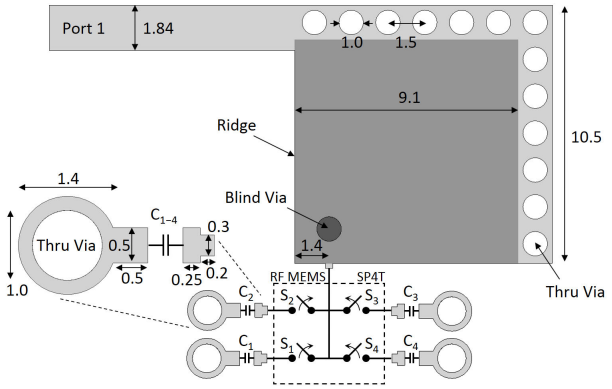


**FIGURE 5.** General schematic with dimensions of the FRQMSIW cavity resonator with packaged RF MEMS SP4T (Analog Devices, Inc. ADG1304) to switch capacitive loading (units in mm). For capacitances $C_{1-4}$, surface mount 0402 ceramic capacitors (Taiyo Yuden UVK Series) are used with values $C_1 = C_2 = C_3 = 2.4$ pF, $C_4 = 1.2$ pF. Light and dark grey areas are the top and embedded ridge metallizations, respectively.

ratio (and therefore cavity miniaturization) between the top and bottom relatively the same [12]. Rogers RO4450F Bondply with 4 mil thickness is used for the bonding layer between substrates. A 50-Ω microstrip feed is again used to weakly couple to the resonator to extract the unloaded resonance frequency $f_0$ and $Q_u$.

An Analog Devices, Inc. ADGM1304 SP4T RF MEMS switch is again used to tune the capacitive loading, and similarly placed on the top metallization of the top substrate, in a location above the peak electric field location. The capacitive loadings are achieved with 0402 surface mount ceramic capacitors (Taiyo Yuden UVK series), which are terminated with through vias shorted to ground. From (4), it can be seen that larger capacitive loadings generate larger resonance frequency shifts. Thus, increased capacitive loading is achieved when more switches are placed in the ON state, where their admittance adds in parallel.

**TABLE 2.** Switch tuning modes and simulated performance of the RF MEMS tunable FRQMSIW cavity with capacitive loading.

| Tuning Mode | S1,S2,S3,S4 | Total Capacitive Loading (pF) | Tuning Element $Q$ | FRQMSIW Cavity $f_0$ (GHz) | FRQMSIW Cavity $Q_u$ |
|---|---|---|---|---|---|
| 1A | 0000 | 0.48 | 125 | 1.080 | 204 |
| 1B | 0001 | 2.51 | 39 | 1.041 | 147 |
| 2A | 0010 | 4.78 | 25 | 0.995 | 90 |
| 2B | 0011 | 7.32 | 23 | 0.942 | 62 |
| 3A | 0110 | 9.32 | 22 | 0.901 | 52 |
| 3B | 0111 | 11.83 | 22 | 0.854 | 46 |
| 4A | 1110 | 14.30 | 18 | 0.811 | 34 |
| 4B | 1111 | 16.72 | 18 | 0.773 | 33 |

In Table 2, the total simulated capacitive loading and $Q$ for each switch state of the tuning element is shown, along with the simulated $f_0$ and $Q_u$ of the capacitively-loaded FRQMSIW cavity. While 16 unique states are possible with the chosen SP4T switch, for this design, 8 unique states are used to allow for a relatively linear change in capacitive loading between tuning modes. This is achieved by having capacitor $C_4$ equal to half the value of each of the other three capacitive loadings. Thus, four broad tuning states are achieved using

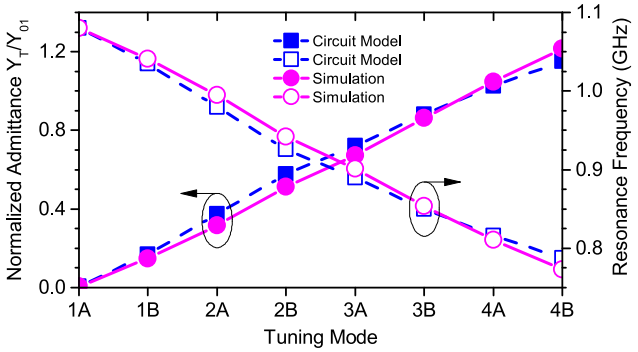


**FIGURE 6.** Change in resonance frequency of a capacitively-loaded FRQMSIW cavity resonator with variation in the normalized admittance for each tuning mode using the circuit model (3) and ADS simulation.

switches S1, S2, and S3, i.e., 000, 001, 011, and 111, while switch S4 toggles a capacitive loading that is approximately halfway between each state.

It is noticed that the tuning element $Q$ decreases with more switches in the ON state, opposite to the effect for the inductive loading in Section III.A. This is due to the parallel resistance of the capacitive loading for each switch effectively adding in parallel when more switches are turned on, decreasing the overall parallel resistance $R_p$ of the total capacitive loading, where $R_p = Q/(\omega C)$ [18]. For tuning mode 1A, with all switches in the OFF state, the FRQMSIW cavity has a $Q_u$ of 204. However, for tuning mode 1B, when switch S4 is turned on, the $Q_u$ of the FRQMSIW cavity drops to 147, and with each additional switch turned on, the $Q_u$ continues to decrease. This again confirms the significant impact of the tuning element $Q$ on the FRQMSIW cavity performance. Still, as mentioned in Section III.A for the inductively-loaded FRQMSIW cavity, the advantages of RF MEMS make them a good choice for design applications requiring high linearity and high power handling.

In Fig. 6, the change in resonance frequency with variation of the normalized total capacitive loading admittance $Y_T/Y_01$ from (3) is plotted for the different tuning modes, along with the simulated case of the loaded FRMQSIW cavity in Fig. 5. From the circuit model, the total shift in resonance frequency is 292 MHz at $f_0 = 934$ MHz, for a tuning range of 31.3%, while for the simulated FRQMSIW cavity, the shift is 307 MHz at $f_0 = 927$ MHz, for a tuning range of 33.1%. Compared to the inductively-loaded case in Fig. 4, we note a larger tuning range and a more linear change in resonance frequency between each state. In addition, good agreement between the circuit model and simulated model is shown, further validating the theory developed in Section II.

## IV. TUNABLE BANDPASS FILTER DESIGN, FABRICATION, AND MEASUREMENT

In this section, both the inductively- and capacitively-loaded FRQMSIW cavities detailed above are used to design RF MEMS tunable bandpass filters (BPF). The fabrication and experimental results of two-pole BPF prototypes using inductive or capacitive loading are presented, while the benefits of each technology are discussed and compared. As a general

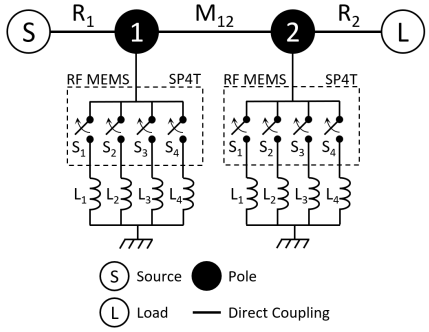


**FIGURE 7.** Coupling routing diagram of a two-pole Chebyshev bandpass filter with RF MEMS switchable inductive loading.

note, the center frequency of each BPF was chosen due to in-house fabrication limitations, thus the operating range of the measured prototypes are presented as a proof-of-concept. However, as previously shown in [12], the FRQMSIW cavity is slightly smaller than even conventional miniaturized microstrip resonators operating at the same resonance frequency, while also having a larger spurious-free region above the passband.

### A. INDUCTIVELY-LOADED FRQMSIW RF MEMS TUNABLE BANDPASS FILTER

In Fig. 7, the coupling routing diagram of an inductively-loaded two-pole FRQMSIW tunable bandpass filter is shown, where resonators #1 and #2 are loaded with RF MEMS SP4T switches to reconfigure their resonance frequency using inductive loadings $L_1$, $L_2$, $L_3$, and $L_4$. From the coupling synthesis of a two-pole Chebyshev bandpass filter, the required normalized coupling coefficient $M_{12}$ and normalized input resistances $R_1$ and $R_2$ can be computed as follows:

$$M_{12} = \frac{1}{\sqrt{g_1 g_2}}, \quad R_1 = \frac{1}{g_0 g_1}, \; R_2 = \frac{1}{g_1 g_2} \tag{6}$$

where $g_0$, $g_1$, $g_2$ and $g_3$ are the Chebyshev lumped-element low-pass prototype elements [19]. The $N + 2$ normalized coupling matrix for a two-pole bandpass filter with 20 dB return loss is then:

$$[M] = \begin{bmatrix} 0 & 1.500 & 0 & 0 \\ 1.500 & 0 & 1.659 & 0 \\ 0 & 1.659 & 0 & 1.500 \\ 0 & 0 & 1.500 & 0 \end{bmatrix} \tag{7}$$

In Fig. 8, the layout of the final design is shown. Rogers RO3010 is used for the top and bottom substrates, with thicknesses of 25 mil and 10 mil, respectively. Adhesives Research EL-7876 2.2 mil thick silicone transfer adhesive tape is used to bond the substrates together.

A standard iris inductive coupling window is used to couple the two resonators, where the dimension $W_{IRIS}$ is mapped to the coupling element $M_{12}$ by simulating two weakly coupled resonators and extracting the coupling coefficient $k$ using the following equations:

$$M = \frac{f_0}{\mathrm{BW}} k, \quad k = \frac{f_e^2 - f_m^2}{f_e^2 + f_m^2} \tag{8}$$

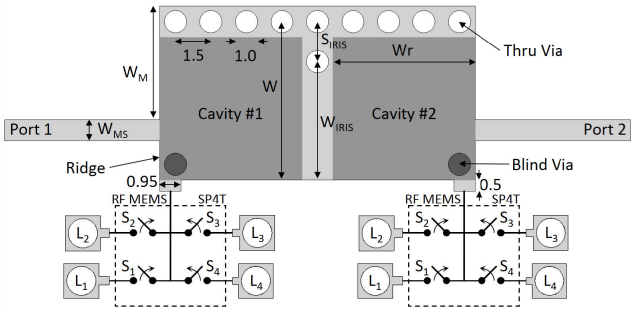


**FIGURE 8.** General schematic of the inductively-loaded two-pole FRQMSIW tunable BPF with $W = 7.1$, $Wr = 6.4$, $W_{IRIS} = 5.3$, $S_{IRIS} = 1.8$, $W_M = 5.1$, and $W_{MS} = 0.95$ (units in mm). Light and dark grey areas are the top and embedded ridge metallizations, respectively.

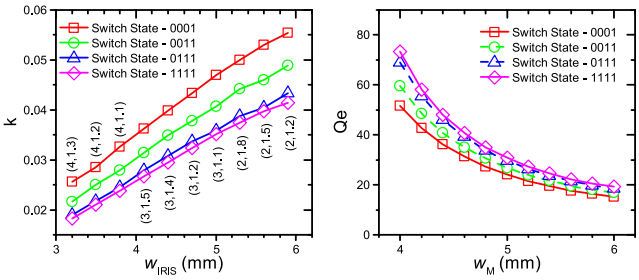


**FIGURE 9.** Simulated extracted (a) coupling coefficient $k$ versus iris window width $W_{IRIS}$, and (b) external quality factor $Q_e$ versus microstrip feed offset $W_M$, for the inductively-loaded FRQMSIW tunable BPF. Within each graph, four different switch states with increasing inductive loading are plotted. The inset coordinates in (a), i.e. (4,1,3), represent the number of coupling vias and via spacing $S_{IRIS}$ (in mm), respectively, to achieve the specific dimension $W_{IRIS}$ shown in the $x$-axis.

where $f_0$ is the center frequency, BW the filter bandwidth, and $f_e$ and $f_m$ the odd-mode (electric) and even-mode (magnetic) resonance frequencies, respectively [17].

In Fig. 9(a), the simulated extracted coupling coefficient $k$ is plotted versus iris dimension $W_{IRIS}$. While the filter is initially designed with a small amount of inductive loading (in this case tuning mode 1B was used), greater inductive loadings perturbate the field distribution within the cavity, and thus impact the amount of coupling between cavities. In Fig. 9(a), when the RF MEMS switch is moved into higher inductively-loaded states, a drop in the amount of coupling is noticed. The effect of decreased coupling is a reduction in bandwidth and increase in passband insertion loss.

Each cavity is fed by a 50-Ω microstrip line connected to the top metallization of the top substrate, and the input/output coupling, controlled by the dimension $W_M$, is determined using the reflection coefficient group delay method [19]. A single microstrip fed cavity is simulated, and the normalized input impedances $R_1$ and $R_2$ are extracted using the equations:

$$R_{1,2} = \frac{\omega_0}{(\omega_2 - \omega_1)} \frac{1}{Q_e}, \quad Q_e = \frac{\omega_0 \tau(\omega_0)}{4} \tag{9}$$

where $(\omega_2 - \omega_1)$ is the filter bandwidth in radians, $Q_e$ is the external quality factor, and $\tau(\omega_0)$ is the reflection group delay at resonance [19].

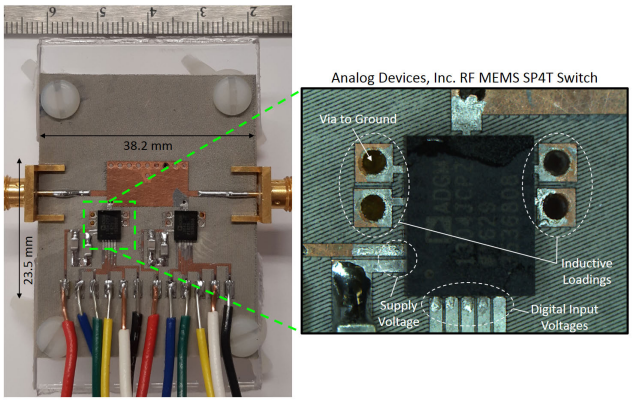


**FIGURE 10.** Picture of the fabricated inductively-loaded two-pole FRQMSIW tunable BPF with packaged RF MEMS SP4T switches (Analog Devices, Inc. ADG1304).

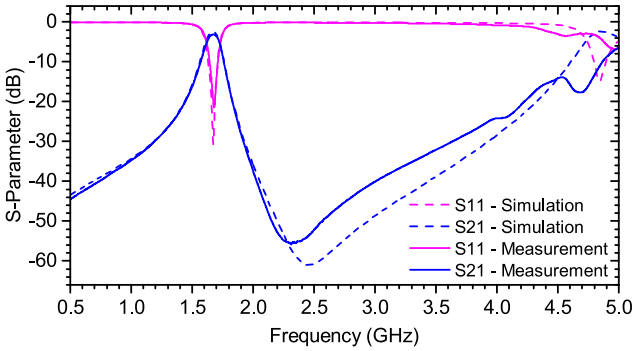


**FIGURE 11.** Measured and simulated scattering parameters of switch tuning mode 1B (see Table 1) for the inductively-loaded two-pole FRQMSIW tunable BPF, showing a wideband spurious-free response.

In Fig. 9(b), the simulated extracted $Q_e$ versus dimension $W_M$ is plotted. Similar to the coupling coefficient, a change in the extracted $Q_e$ at a fixed dimension $W_M$ is noted as the inductive loading is increased. Due to the change in field distribution, the amount of energy coupled into the cavity is decreased with greater loading, decreasing the return loss.

After a last optimization in ADS, the final dimensions of the filter are shown in Fig. 8, where each RF MEMS chip has similar inductive loading dimensions and values as for the single resonator in Section III.A. In Fig. 10, a picture of the fabricated filter is shown, including a close-up of the RF MEMS SP4T switch and inductive loadings. The total area of the filter is 23.5 mm by 38.2 mm.

The measured and simulated scattering parameters for tuning mode 1B are plotted in Fig. 11. For the simulated filter (ADS), the insertion loss is 2.55 dB at resonance frequency $f_0 = 1.670$ GHz, with 1-dB and 3-dB bandwidths of 77 MHz and 124 MHz (fractional bandwidths of $\text{FBW}_{\text{1-dB}} = 4.6\%$ and $\text{FBW}_{\text{3-dB}} = 7.4\%$), respectively. For the measured filter, the insertion loss is 3.10 dB at resonance $f_0 = 1.675$ GHz, with 1-dB and 3-dB bandwidths of 75 MHz and 123 MHz ($\text{FBW}_{\text{1-dB}} = 4.5\%$ and $\text{FBW}_{\text{3-dB}} = 7.4\%$), respectively. The return loss for both measured and simulated is greater than 20 dB. The shift in simulated versus measured resonance frequency is only 0.3%, showing good modelling accuracy of the RF MEMS chips and inductive loadings.

A wide spurious-free region is also noted in Fig. 11. In [12], it was shown for FRQMSIW cavities that the ratio between the 1st and 2nd order resonances is approximately 1:5. Due to the loading being entirely inductive, no additional resonances are introduced. Thus, for the inductively-loaded FRQMSIW RF MEMS tunable BPF, the large spurious-free region above the filter passband of the FRQMSIW cavity is maintained.

In Fig. 12, the measured filter performance for three of the main tuning modes 1B, 2B, and 3D are shown, with the inset plotting the finer tuning modes 3A to 3D. The total frequency tuning range is from 1.675 GHz to 1.750 GHz, for a tuning bandwidth of 75 MHz, or 4.4%, with respect to a center frequency of 1.713 GHz, again noting that tuning mode 0A is not used due to the significant jump from capacitive (all switches in OFF state) to inductive loading. The low tuning range is due to the difficulty of achieving small inductive loading values in practice, which are necessary for high tuning ranges as determined in (3). The conductive through via themselves are inductive [17], thus a very short microstrip line was used for each loading. Furthermore, some fabrication errors led to a poor connection between the RF MEMS chip and one of the inductive loadings, thus the full tuning range was not possible in measurement. The insertion loss varies between 3.10 dB to 3.92 dB. The high insertion loss with small loading is likely due to the fabrication bonding layer. The increase in insertion loss with greater loading is likely due to the conductive through via used for inductive loading. A small amount of additional loss is incurred when more switches are in the ON state, however the reported insertion loss of the Analog Devices, Inc. RF MEMS SP4T switch ADGM1304 is less than 0.26 dB below 2.5 GHz [16]. The return loss for all measured states is above 15 dB.

In Fig. 13, both the 1-dB and 3-dB bandwidths and FBWs are plotted for the main tuning modes 1B, 2B, and 3D. The 1-dB and 3-dB bandwidths range from 67.3 MHz ±7.2 MHz and 112.7 MHz ±10.2 MHz, respectively, where the fractional bandwidths are $\text{FBW}_{\text{1-dB}} = 3.96\% \pm 0.51\%$ and $\text{FBW}_{\text{3-dB}} = 6.62\% \pm 0.73\%$. While a small shift in bandwidth is noted across the tuning range, the shift in FBW is slightly greater since the resonance frequency increases with greater inductive loading ($\text{FBW} = \Delta f / f_0$). To improve the design for constant bandwidth across the tuning range, the thickness of the coupling through vias can be optimized by choosing a smaller drill diameter. For this work, the available in-house fabrication tools limited the choice to 1 mm via diameters, but diameters as low as 0.25 mm or less are possible in industrial PCB fabrication facilities.

The measured average unloaded quality factor $Q_u$ can be extracted using the formula:

$$Q_u = \frac{27.3 \times f_0 \times \tau(f_0)}{|S_{21}(f_0)|} \tag{10}$$

where $f_0$ is the resonance frequency (in GHz), $\tau(f_0)$ is the group delay of $S_{21}$ at $f_0$ (in ns), and $|S_{21}(f_0)|$ is the insertion loss at $f_0$ (in dB) [20]. For the measured filter, the average $Q_u$

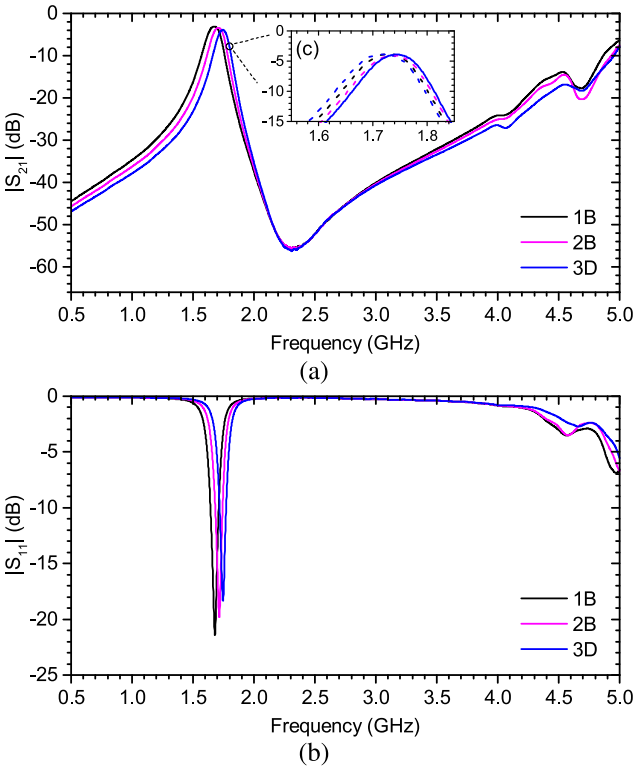


**FIGURE 12.** Measured (a) power transmission ($|S_{21}|$) and (b) power reflection ($|S_{11}|$) responses of switch tuning modes 1B, 2B, and 3D (see Table 1) for the inductively-loaded two-pole FRQMSIW tunable BPF, where inset (c) shows finer tuning within broad switch tuning mode group 3A-3D (left to right).

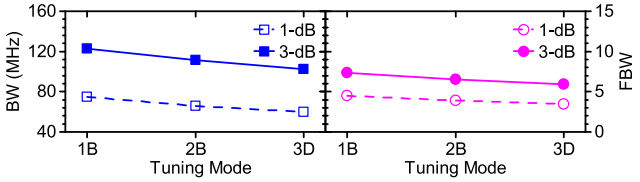


**FIGURE 13.** Measured 1-dB and 3-dB BW and FBW of the inductively-loaded two-pole FRQMSIW tunable BPF for main switching states 1B, 2B, and 3D.

ranges from 90 to 54, with the largest value when all switches are in the OFF state.

### B. CAPACITIVELY-LOADED FRQMSIW RF MEMS TUNABLE BANDPASS FILTER

In Fig. 14, the coupling routing diagram of a capacitively-loaded two-pole FRQMSIW tunable bandpass filter is shown. Similar to the inductively-loaded case, the resonance frequency of resonators #1 and #2 are each tuned by an RF MEMS SP4T switch, which reconfigures the total capacitive loading of $C_1$, $C_2$, $C_3$, and $C_4$. The required normalized coupling coefficient $M_{12}$ and normalized input resistances $R_1$ and $R_2$ are determined using (10), where the $N+2$ normalized coupling matrix for 20 dB return loss is shown in (7).

Fig. 15 shows the final design layout, where each RF MEMS chip has similar capacitive loading dimensions and values as for the single cavity in Fig. 5. Rogers RO3010 is used for the top and bottom substrates, with thicknesses of 50 mil and 25 mil, respectively. As for the single

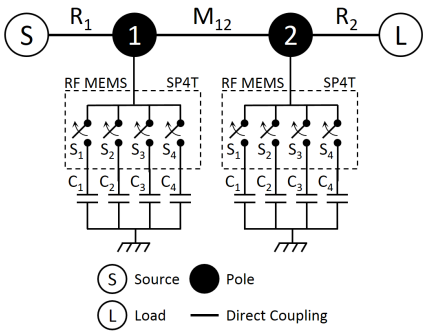


**FIGURE 14.** Coupling routing diagram of a two-pole Chebyshev bandpass filter with RF MEMS switchable capacitive-loading.

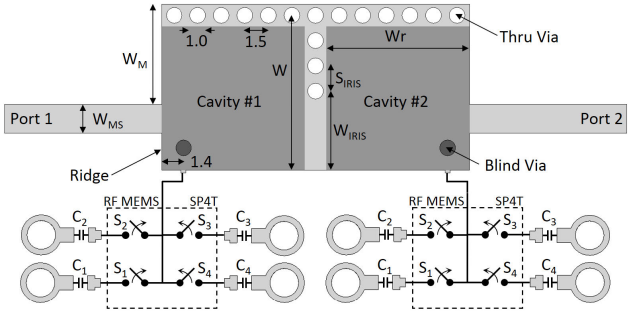


**FIGURE 15.** General schematic of the capacitively-loaded two-pole FRQMSIW tunable BPF, with $W = 9.8$, $Wr = 9.1$, $W_{IRIS} = 5$, $S_{IRIS} = 1.6$, $W_M = 6.34$, and $W_{MS} = 1.84$ (units in mm). Light and dark grey areas are the top and embedded ridge metallizations, respectively.

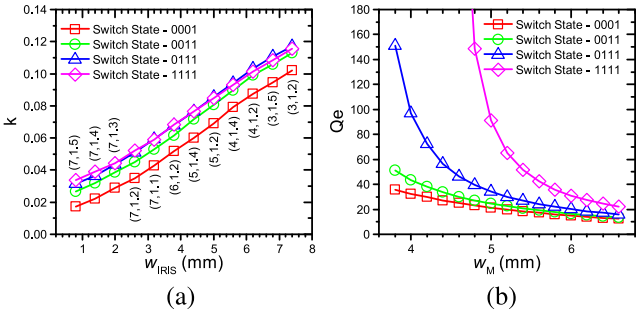


**FIGURE 16.** Simulated extracted (a) coupling coefficient $k$ versus iris window width $W_{IRIS}$, and (b) external quality factor $Q_e$ versus microstrip feed offset $W_M$, for the capacitively-loaded FRQMSIW tunable BPF. For each plot, four different switch states with increasing inductive loading are included. The inset coordinates in (a), i.e. (7, 1.5), represent the number of coupling vias and via spacing $S_{IRIS}$ (in mm), respectively, to achieve the specific dimension $W_{IRIS}$ shown in the $x$-axis.

capacitively-loaded cavity design in Section III.B, thicker substrates are chosen while maintaining a similar ratio between the top and bottom substrate thicknesses to improve insertion loss [12]. Rogers RO4450F bondply with 4 mil thickness is used to bond the substrates together.

A standard iris inductive coupling window is used to couple the two resonators, where the dimension $W_{IRIS}$ can be mapped to the required $M_{12}$ by (8). In Fig. 16(a), the extracted coupling coefficient $k$ versus coupling dimension $W_{IRIS}$ is plotted. It is noticed that the change in the coupling coefficient between switch state 0001 and 1111 remains relatively constant across the entire range of $W_{IRIS}$. Furthermore, opposite to the inductively-loaded case, greater coupling is achieved with greater capacitive loading. This is likely due

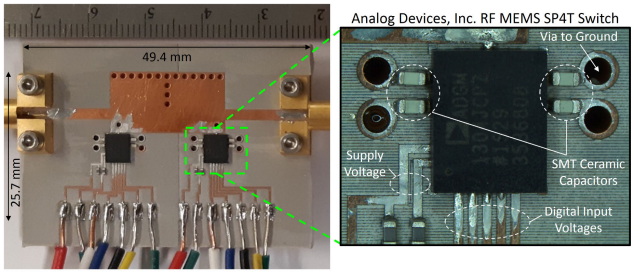


**FIGURE 17.** Picture of the fabricated capacitively-loaded two-pole FRQMSIW tunable BPF with packaged RF MEMS SP4T switches (Analog Devices, Inc. ADG1304).

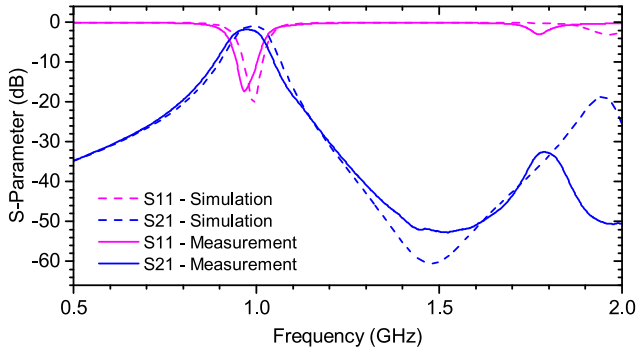


**FIGURE 18.** Measured and simulated scattering parameters of switch tuning mode 1B (see Table 2) for the capacitively-loaded two-pole FRQMSIW tunable BPF.

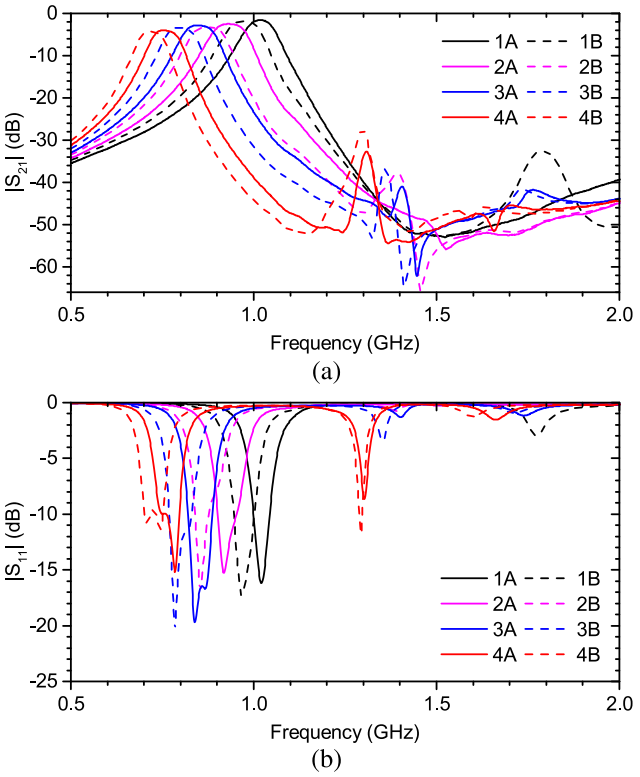


**FIGURE 19.** Measured (a) power transmission ($|S_{21}|$) and (b) power reflection ($|S_{11}|$) responses of the capacitively-loaded two-pole FRQMSIW tunable BPF for all switch tuning states.

to increased field concentration within the capacitive ridge region, increasing the amount of coupling between the two resonators.

A 50-Ω microstrip line is used to feed the two cavities, connected to the top metallization layer of the top substrate. The required input/output coupling is determined by mapping the normalized input impedances $R_1$ and $R_2$ to the dimension $W_M$ using (9). In Fig. 16(b), the extracted $Q_e$ versus $W_M$ is plotted. Similar to the inductively-loaded case, a change in $Q_e$ is noticed for greater loading states, where the amount of energy coupled into the cavity decreases. This is again likely due to a perturbation in field distribution with increased loading. As the dimension $W_M$ increases, this effect becomes less noticeable.

A last design optimization is performed in ADS, and the final dimensions are shown in Fig. 15. A picture of the fabricated filter is shown in Fig. 17. Due to the increased thickness of the substrates, Rosenberger 32K243-40ML5 SMA clamp connectors were used to connect to the filter. The total area of the filter is 25.7 mm by 49.4 mm.

In Fig. 18, the measured and simulated scattering parameters for tuning mode 1B are plotted, showing good agreement. For the simulated filter, the insertion loss is 0.96 dB at resonance frequency $f_0 = 990$ MHz, with 1-dB and 3-dB bandwidths of 62 MHz and 96 MHz ($\text{FBW}_{\text{1-dB}} = 6.3\%$ and $\text{FBW}_{\text{3-dB}} = 9.7\%$), respectively. For the measured filter, the insertion loss is 1.80 dB at resonance frequency $f_0 = 974$ MHz, with 1-dB and 3-dB bandwidths of 65 MHz and 99 MHz ($\text{FBW}_{\text{1-dB}} = 6.7\%$ and $\text{FBW}_{\text{3-dB}} = 10.2\%$), respectively. Both measured and simulated return loss is greater than 17 dB. The shift between simulated and measured resonance frequency is 1.6%, again showing good modelling accuracy of the RF MEMS chip with capacitive loading. While slightly larger than the inductively-loaded filter, this is likely caused by parasitic effects due to soldering of the surface mount capacitors, altering the loading on the filter. Furthermore, a 1.3 dB decrease in measured insertion loss compared to the inductively-loaded filter with the same tuning mode (1B) is achieved. This improved performance is attributed to the thicker substrates and choice of bonding layer with lower dielectric loss.

In Fig. 19, the measured filter performance is plotted for each of the 8 tuning states. The frequency tuning range is from 713 MHz to 1.017 GHz, for a tuning bandwidth of 305 MHz, or 35.2%, with respect to a center frequency of 865 MHz. The insertion loss varies between 1.59 dB to 4.29 dB, while the return loss is above 10 dB for each tuning state. The higher insertion loss at greater capacitive loadings is likely due to the losses incurred in the surface mount capacitors and conductive through vias, i.e., when more switches are in the ON state. A decrease in the spurious-free region above the passband is also noticed with greater capacitive loading. Since each load has effectively a capacitor in series with an inductor (conductive through via), an additional resonance occurs above the passband, decreasing the spurious-free region compared to the inductively-loaded BPF.

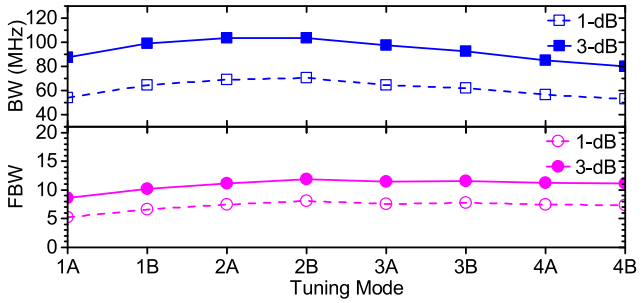


**FIGURE 20.** Measured 1-dB and 3-dB BW and FBW of the capacitively-loaded two-pole FRQMSIW tunable BPF for all switch tuning states.

In Fig. 20, the 1-dB and 3-dB bandwidths and FBWs are plotted for all tuning modes. The 1-dB and 3-dB bandwidths range from 61.8 MHz ±8.7 MHz and 91.8 MHz ±11.9 MHz, respectively, where the fractional bandwidths are $FBW_{1\text{-dB}} = 7.72\% \pm 0.34\%$ and $FBW_{3\text{-dB}} = 11.47\% \pm 0.39\%$. While the relative change in bandwidth is greater compared to the inductively-loaded BPF, the change in FBW is decreased. This is due to the resonance frequency decreasing with increased capacitive loading, while for the inductively-loaded case, the resonance frequency increased with greater loading. Thus, the FBW remains relatively stable across the entire tuning range for the capacitively-loaded BPF.

The measured extracted $Q_u$ for the capacitively-loaded BPF ranges from 92 to 27, with the largest value when all switches are in the OFF state, and the lowest value when all switches are in the ON state. A greater swing in $Q_u$ is noticed compared to the inductively-loaded BPF, as expected from the discussion in Section III where the tuning element $Q$ decreases with more switches turned on. Furthermore, greater field concentration within the ridge region as the capacitive loading is increased is also expected to decrease $Q_u$.

## V. FINAL DISCUSSION

In Table 3, the performance of the measured inductively-loaded and capacitively-loaded FRQMSIW filters are shown, along with the RF MEMS tunable HMSIW filter in [14] and RF MEMS tunable SIW filter in [13]. While a small tuning range of 4.4% is achieved for the inductively-loaded case of the FRQMSIW, the tuning range of 35.2% for the capacitively-loaded case is greater than both the HMSIW and SIW tunable filters. With respect to free-space lambda at each filters center frequency, the inductively-loaded FRQMSIW filter of this work achieves a miniaturization of 70.3% compared to the HMSIW, and 88.0% compared to the SIW, while the capacitively-loaded FRQMSIW achieves a miniaturization of 78.8% compared to HMSIW, and 91.4% compared to the SIW. This is a substantial amount of miniaturization, considering the RF MEMS tunable HMSIW filter in [14] is reported to be $\sim$ 2.5 times smaller than the tunable standard SIW filter in [13]. Furthermore, the significant miniaturization of the capacitively-loaded tunable FRQMSIW filter compared to the standard tunable SIW filter is achieved while also improving the filters measured insertion loss.

**TABLE 3.** SIW-based RF MEMS tunable filter performance comparison.

| SIW Technology | Loading Type | Frequency Shift (GHz) | Tuning Range | Total Area | Miniat-urization | |
|---|---|---|---|---|---|---|
| FRQMSIW | Capacitive | $0.713 - 1.017$ | 35.2% | $0.004\times\lambda_0$ | 91.4% | This Work |
| FRQMSIW | Inductive | $1.675 - 1.750$ | 4.4% | $0.005\times\lambda_0$ | 88.0% | This Work |
| HMSIW | Inductive | $1.2 - 1.6$ | 28% | $0.017\times\lambda_0$ | 59.4% | [14] |
| SIW | Tuning Post | $1.2 - 1.6$ | 28% | $0.043\times\lambda_0$ | Ref. | [13] |

**TABLE 4.** Tunable bandpass filter comparison for different resonator technologies and tuning elements.

| Technology | Tuning Element | Center Freq. (GHz) | Tuning Range | Insertion Loss (dB) | $Q_u$ | |
|---|---|---|---|---|---|---|
| FRQMSIW | RF MEMS | 0.87 | 35% | 1.6−4.3 | 92−27 | This Work |
| HMSIW | Varactor | 1.31 | 30% | 7.0−2.62 | 31−168 | [21] |
| Microstrip | Varactor | 0.94 | 34% | 4.3−1.9 | 30−75 | [22] |
| Microstrip | RF MEMS | 6.15 | 28% | 4.8−5.3 | Not Reported | [23] |

In Table 4, the performance of the capacitively-loaded FRQMSIW filter is shown versus other tunable planar filter technologies using RF MEMS or varactor diodes. Comparable performance is achieved between the different technologies and tuning elements, where the higher insertion loss of all the reported filters is mainly due to the Q of the tuning element, and not the unloaded resonators of the various technologies themselves. In addition to the miniaturization potential of the FRQMSIW cavity compared to other SIW-based resonators such as the HMSIW in [21], the authors previously reported a smaller footprint for the unloaded FRQMSIW cavity compared to conventional miniaturized microstrip meander open-loop resonators [12]. For the performance of the tuning elements themselves, RF MEMS typically achieve higher linearity and lower insertion losses compared to varactors [2], [23].

The tunable FRQMSIW cavity presented here also has the potential to be used as a building block in even higher order reconfigurable filters. In addition to tuning the resonance frequency, the authors anticipate the possibility for placing the RF MEMS switchable loading in locations such that the coupling between cavities or input coupling can be tuned. This would allow tuning of the filter bandwidth along with the center frequency, and in higher order filters with cross-couplings, tuning of transmission zeros.

## VI. CONCLUSION

The design of both inductively- and capacitively-loaded RF MEMS tunable FRQMSIW bandpass filters has been presented. Significant miniaturization is achieved for both inductively- and capacitively-loaded cases, with 70.3% and 78.8% reductions in filter area, respectively, compared to a similar RF MEMS tunable filter using HMSIW technology. An analytic theory is developed to calculate the shift in resonance frequency of a reactively loaded FRQMSIW cavity. Two filter prototypes are measured, with the inductively-loaded bandpass filter achieving 4.4% tuning range with respect to 1.713 GHz center frequency, and the capacitively-loaded bandpass filter achieving 35.2% tuning range with respect to 865 MHz center frequency. This work

highlights the potential for FRQMSIW cavities loaded with RF MEMS tunable elements in miniaturized tunable bandpass filter design.

## ACKNOWLEDGMENT

The authors wish to thank Eric Carty from Analog Devices, Inc., for his generous donation and technical discussions related to the RF MEMS SP4T ADGM1304 switches used in this research. They also wish to thank Adhesives Research for providing the EL-7876 silicone transfer adhesive tape. This work is dedicated to the memory of Professor Mojgan Daneshmand, who passed away on January 8, 2020.

## REFERENCES

[1] G. M. Rebeiz, K. Entesari, I. C. Reines, S.-J. Park, M. A. El-Tanani, A. Grichener, and A. R. Brown, "Tuning in to RF MEMS," *IEEE Microw. Mag.*, vol. 10, no. 6, pp. 55–72, Oct. 2009.

[2] K. Entesari and G. M. Rebeiz, "RF MEMS, BST, and GaAs varactor system-level response in complex modulation systems," *Int. J. RF Microw. Comput.-Aided Eng.*, vol. 18, no. 1, pp. 86–98, Jan. 2008.

[3] D. Peroulis, E. Naglich, M. Sinani, and M. Hickle, "Tuned to resonance," *IEEE Microw. Mag.*, vol. 15, no. 5, pp. 55–69, Aug. 2014.

[4] X.-P. Chen and K. Wu, "Substrate integrated waveguide filter: Basic design rules and fundamental structure features," *IEEE Microw. Mag.*, vol. 15, no. 5, pp. 108–116, Jul. 2014.

[5] W. Hong, B. Liu, Y. Wang, Q. Lai, H. Tang, X. X. Yin, Y. D. Dong, Y. Zhang, and K. Wu, "Half mode substrate integrated waveguide: A new guided wave structure for microwave and millimeter wave application," in *Proc. Joint 31st Int. Conf. Infr. Millim. Waves 14th Int. Conf. THz Electron.*, Shanghai, China, Sep. 2006, p. 219.

[6] S. Moscato, C. Tomassoni, M. Bozzi, and L. Perregrini, "Quarter-mode cavity filters in substrate integrated waveguide technology," *IEEE Trans. Microw. Theory Techn.*, vol. 64, no. 8, pp. 2538–2547, Aug. 2016.

[7] N. Grigoropoulos, B. Sanz-Izquierdo, and P. R. Young, "Substrate integrated folded waveguides (SIFW) and filters," *IEEE Microw. Wireless Compon. Lett.*, vol. 15, no. 12, pp. 829–831, Dec. 2005.

[8] L.-S. Wu, J. Mao, and W.-Y. Yin, "Compact quasi-elliptic bandpass filter based on folded ridge substrate integrated waveguide (FRSIW)," in *Proc. Asia–Pacific Microw. Conf.*, Kaohsiung, Taiwan, Dec. 2012, pp. 385–387.

[9] T. R. Jones and M. Daneshmand, "The characterization of a ridged half-mode substrate-integrated waveguide and its application in coupler design," *IEEE Trans. Microw. Theory Techn.*, vol. 64, no. 11, pp. 3580–3591, Nov. 2016.

[10] T. R. Jones, M. H. Zarifi, and M. Daneshmand, "Miniaturized quarter-mode substrate integrated cavity resonators for humidity sensing," *IEEE Microw. Wireless Compon. Lett.*, vol. 27, no. 7, pp. 612–614, Jul. 2017.

[11] T. R. Jones and M. Daneshmand, "Miniaturized folded ridged half-mode substrate integrated waveguide," in *Proc. 47th Eur. Microw. Conf. (EuMC)*, Nuremberg, Germany, Oct. 2017, pp. 528–531.

[12] T. R. Jones and M. Daneshmand, "Miniaturized folded ridged half-mode and quarter-mode substrate integrated waveguides for filter design," *IEEE Trans. Microw. Theory Techn.*, vol. 67, no. 8, pp. 3413–3426, Aug. 2019.

[13] V. Sekar, M. Armendariz, and K. Entesari, "A 1.2–1.6-GHz substrate-integrated-waveguide RF MEMS tunable filter," *IEEE Trans. Microw. Theory Techn.*, vol. 59, no. 4, pp. 866–876, Apr. 2011.

[14] V. Sekar and K. Entesari, "A half-mode substrate-integrated-waveguide tunable filter using packaged RF MEMS switches," *IEEE Microw. Wireless Compon. Lett.*, vol. 22, no. 7, pp. 336–338, Jul. 2012.

[15] T. R. Jones and M. Daneshmand, "Miniaturized reconfigurable dual-band bandstop filter with independent stopband control using folded ridged quarter-mode substrate integrated waveguide," in *IEEE MTT-S Int. Microw. Symp. Dig.*, Boston, MA, USA, Jun. 2019, pp. 102–105.

[16] Analog Devices. *Data Sheet ADGM1304*. Accessed: Jul. 21, 2019. [Online]. Available: https://www.analog.com/media/en/technical-documentation/data-sheets/adgm1304.pdf

[17] M. E. Goldfarb and R. A. Pucel, "Modeling via hole grounds in microstrip," *IEEE Microw. Guided Wave Lett.*, vol. 1, no. 6, pp. 135–137, Jun. 1991.

[18] G. M. Rebeiz, *RF MEMS Theory, Design, and Technology*. Hoboken, NJ, USA: Wiley, 2003.

[19] R. J. Cameron, R. Mansour, and C. M. Kudsia, *Microwave Filters for Communication Systems: Fundamentals, Design and Applications*, 2nd ed. Hoboken, NJ, USA: Wiley, 2018.

[20] G. L. Matthaei, L. Young, and E. M. T. Jones, "Sec. 6.15, group delay," in *Design of Microwave Filters, Impedance-Matching Networks, and Coupling Structures*. New York, NY, USA: McGraw-Hill, 1964, pp. 339–348.

[21] B. You, S. Lu, L. Chen, and Q. J. Gu, "A half-mode substrate-integrated filter with tunable center frequency and reconfigurable bandwidth," *IEEE Microw. Wireless Compon. Lett.*, vol. 26, no. 3, pp. 189–191, Mar. 2016.

[22] Y.-H. Cho and G. M. Rebeiz, "Two- and four-pole tunable 0.7–1.1-GHz bandpass-to-bandstop filters with bandwidth control," *IEEE Trans. Microw. Theory Techn.*, vol. 62, no. 3, pp. 457–463, Mar. 2014.

[23] T.-W. Lin, K. K. W. Low, R. Gaddi, and G. M. Rebeiz, "High-linearity 5.3–7.0 GHz 3-pole tunable bandpass filter using commercial RF MEMS capacitors," in *Proc. 48th Eur. Microw. Conf. (EuMC)*, Madrid, Spain, Sep. 2018, pp. 555–558.

**THOMAS R. JONES** (Member, IEEE) received the B.Sc. and Ph.D. degrees in electrical and computer engineering from the University of Alberta, in 2007 and 2019, respectively.

From 2008 to 2013, he was with Tracer Industries Canada Ltd., Edmonton, as a Project Engineer. In 2013, he joined the Microwave to Millimeter-Wave Group, University of Alberta, where he is currently a Postdoctoral Fellow. He is also a Visiting Postdoctoral Scholar with Purdue University. His current research interests include RF- and millimeter-wave tunable filter design for wireless and satellite communication systems, reconfigurable RF front ends for 5G, and the microfabrication of monolithically integrated waveguide devices.

Dr. Jones was a recipient of the Queen Elizabeth II Graduate Scholarship, the Alberta Innovates Technologies Futures (AITF) Graduate Student Scholarship, the Natural Science and Engineering Research Council (NSERC) Alexander Graham Bell Canada Graduate Scholarship, and the NSERC Postdoctoral Fellowship. He served as the Finance Chair of the 2019 IEEE Canadian Conference on Electrical and Computer Engineering (CCECE), while currently serving as the Vice-Chair of the award-winning IEEE Northern Canada Section AP-S/MTT-S Joint Chapter.

**MOJGAN DANESHMAND** (Senior Member, IEEE) received the B.Sc. degree from the Iran University of Science and Technology (IUST), in 1999, the M.Sc. degree from the University of Manitoba, in 2001, and the Ph.D. degree from the University of Waterloo, in 2006, all in electrical engineering.

She is currently a Professor with the University of Alberta, with a research focus on radio frequency (RF) microsystems for communication and sensing. She applies RF sensing and communication to energy systems, wireless and satellite payloads, and biomedical devices. Her group has pioneered works on advanced satellite and wireless RF front end systems, and non-contact microwave sensing. She has published her research results in more than 150 publications and holds several patents.

Dr. Daneshmand was the recipient of the 2016 IEEE AP-S Lot Shafai Mid-Career Distinguished Achievement Award for her scientific contribution to the fields of microwave communication and sensing technologies and being a role model for women in engineering and the 2018 Martha Cook Piper Research Prize from the University of Alberta for outstanding promise as a researcher. Her group has garnered a range of awards, including the IEEE AP-S, the IEEE IMS, and CMC paper awards and recognitions. She is the Co-Chair of the award-winning IEEE Northern Canada Section AP-S/MTT-S Joint Chapter and is also a member of the IEEE IMS Conference Technical Program Review Committee (TPRC). She was an Associate Editor of the IEEE CANADIAN JOURNAL OF ELECTRICAL AND COMPUTER ENGINEERING, from 2014 to 2016. She is an Associate Editor of the IEEE TRANSACTIONS ON ANTENNAS AND PROPAGATION.